13th ewtec 2019 Proceedings of the 13th European Wave and Tidal Energy Conference 1-6 Sept 2019, Naples, Italy

Linear analysis of fluid-filled membrane structures using generalised modes

Anthony McDonald, Qing Xiao, David Forehand, and Ronan Costello

***Abstract*—A frequency domain model is developed for the analysis of the fluid-structure interaction of surface gravity waves with a fluid-filled membrane. The membrane structure shape under static load conditions is first calculated using a non-linear quasi-static finite element method. Generalised modes are then used to couple the effect of the external fluid and incident waves with the response of the membrane structure and the internal fluid. The system is then solved in the frequency domain. The model builds on existing theory where possible, while the use of generalised modes allows different mode types to be used depending on what is appropriate for the analysis. Results computed for a bottom-mounted fluid-filled membrane are compared with previous numerical and experimental results.**

***Index Terms*—Hydroelasticity, generalised modes, fluid-filled membranes, boundary element method, finite element method**

I. Introduction

FLUID-filled flexible membrane devices have been used, or are proposed to be used, in the marine environment for a range of applications. These applications include flexible breakwaters [1], fluid storage/transportation systems [2], fish farms [3], and wave energy converters (WECs) [4]. It is flexible membrane WECs that are of particular interest here. WECs which utilise flexible membranes "have the potential to enable a radically different type of WEC structure to those that have been trialled at full scale to date" which could lead to "an overall step change in cost" [5]. However, there is no generic method or tool for analysis of flexible membrane WECs, which is a barrier to the analysis of new concepts or investigation of the design space. This paper extends the work in [6] focusing on the development of a model for analysis of a generic fluid-filled membrane structure, so does not deal with the power take-off (PTO) that would be present in a WEC or the option of the internal domain being air-filled rather than fluid-filled.

A number of numerical models have been developed for the analysis of fluid-filled membrane structures. In general, the numerical models consist of a boundary element method (BEM) model to determine the dynamic pressure of the external and internal fluid on the membrane using the assumption of linear potential flow, and a membrane structural model that is solved for membrane displacements. Ohyama et al. [1] modelled the internal and external domain in 2D using the BEM and approximated the membrane as a series of linear springs. Zhao [7], again using the BEM for the internal and external domains, used a formulation based on the balance of hoop tension with the pressure difference across the membrane. Zhao and Aarsnes [8] extended this model by including the effect of membrane elasticity. Phadke and Cheung [9] derived the membrane equation of motion from the membrane theory of shells and set up analysis using the finite element method which was coupled with the BEM for the fluid domains. Broderick and Leonard [10] developed a model including non-linear effects in the time domain. However, the internal domain was dealt with using a lumped mass method. Phadke and Cheung [11] later developed a non-linear model where both the internal and external domain was analysed using the boundary element method.

In each of these fluid-filled membrane models, the coupling between fluid and structure is performed at a nodal level, which does not allow for ease of integration with existing hydrodynamic BEM codes and requires the development of a bespoke finite element analysis (FEA) tool. Analysis of ultra large container ships, however, requires a similar hydroelastic analysis (without the presence of the internal fluid) and it has been performed using generalised modes [12]. This allows for the use of existing FEA and BEM tools.

The use of generalised modes means that a modal hydroelastic restoring stiffness is needed for the analysis. The linear formulation for rigid body hydrostatics restoring stiffness is well-known [13] and developed from the calculation of first-order forces on a body due to hydrostatic pressure over the body and the body self-weight. The extension of the hydrostatic stiffness terms to generalised modes should also contain all first-order variations of forces associated with the initial equilibrium configuration and so should also include the well known rigid body hydrostatic stiffness matrix as a special case when rigid body modes are used.

A number of methods have been proposed for determining the restoring stiffness of hydroelastic structures, but as of yet, there is no consensus on the correct method. The consistent hydroelastic stiffness method [14] is based on the contributions of the hydrostatic pressure and the body self-weight and is similar to the rigid body restoring stiffness. The complete method is developed by consistent linearization of the external

ID: 1487, Track: WDD. This work was funded by Wave Venture, the Energy Technology Institute and the Research Council Energy Programme as part of the IDCORE program under grant EP/J500847

A. McDonald is with the Industrial Doctoral Centre for Offshore Renewable Energy (e-mail: a.mcdonald@ed.ac.uk).

Q. Xiao is at the Department of Naval Architecture, University of Strathclyde, Glasgow, UK (e-mail: qing.xiao@strath.ac.uk).

D. Forehand is at the Institute of Energy Systems, University of Edinburgh, Edinburgh, UK (e-mail: d.forehand@ed.ac.uk).

R. Costello is at Wave Venture, Truro, UK (e-mail: ronan@waveventure.com).

and internal generalised forces. While the unified hydroelastic stiffness method [15] combines the consistent method with the contribution due to the geometric stiffness (from the complete method) and removes terms that are common to both. However, the unified method can be simplified to the complete hydroelastic stiffness method [16] by the assumption of a thin-walled structure.

In this paper, a model is described that uses the generalised mode method to analyse a fluid-filled membrane structure. In this model the static shape analysis is performed using standard non-linear quasi-static FEA. The external and internal domain analysis is performed using a modified version of linear potential flow BEM solver Nemoh [17], and the complete hydroelastic method [16] is used to determine the restoring stiffness of the membrane generalised mode shapes. A test-case is then presented for a bottom-mounted fluid-filled membrane structure and the model results are compared with results from numerical and experimental studies.

II. Static shape analysis

A membrane is a thin-walled structure which can only carry internal tension forces tangential to the membrane surface. It cannot support bending or torsion moments, or compressive forces. As a result, a membrane surface adapts to external loads by a combination of in-plane tension and shape deformation and has no unique shape in the absence of loads. For dynamic motion analysis to take place the shape and static stress of the membrane structure under static loading conditions must first be determined.

An initial unstressed shape must be assumed, based on the unstressed membrane dimensions and the anticipated stressed shape. Then the deformation away from this initial unstressed shape can be calculated by considering the equilibrium of internal and external forces on the membrane. This deformation can be large compared with the thickness of the membrane so that the pressure loads cannot be assumed to be applied on the undeformed surface. Additionally, large strains can be present such that a linear stress-strain relationship cannot be assumed. As a result, a generic code necessitates the use of non-linear analysis.

The Code Aster FEA tool [18] is used for quasi-static non-linear mechanical analysis of hyperelastic membranes. A mesh of the unstressed shape (S_0 in Fig. 1) is input to Code Aster, along with the membrane material parameters, the edge constraints, and gravity and pressure loads. The pressure loads are the internal and external hydrostatic pressures and any additional overpressure (P_0) in the internal domain (Ω_{int}). If the device is fully submerged and the fluid density is the same in the internal domain as the external domain, then the internal and external hydrostatic pressure cancel and do not need to be included in the FEA model. However, if hydrostatic pressure loading must be included in the model then a development branch of Code Aster, created by the authors, must currently be used to allow for the inclusion of a pressure that varies as a function of depth and follows the deformation of the surface throughout the simulation.

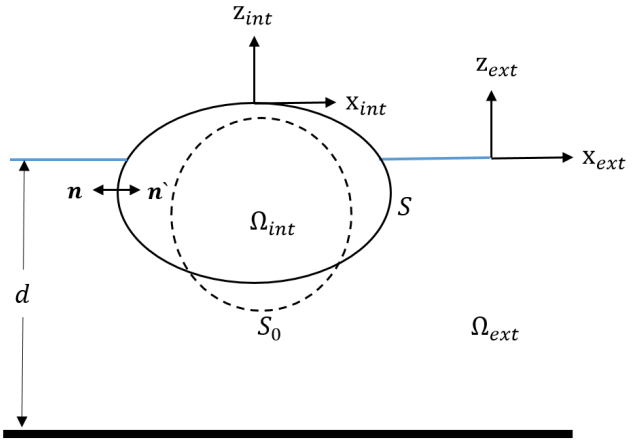

Fig. 1. Definition sketch for fluid-filled membrane.

Two hyperelastic material laws are built into Code Aster. The Neo-Hookean model (a special case of the Mooney-Rivlin model) is used as it has been found to produce better results than the Saint Venant-Kirchhoff model. However, the Neo-Hookean model is not valid for very large strains. The validity of the Neo-Hookean model decreases as the critical strain (where the strain increases rapidly with a reduction in stress) is approached, and the model is unstable beyond this point. In this situation, the quasi-static non-linear Newton solver cannot converge on a solution. A more accurate model (such as the Mooney-Rivlin model) would be required to capture this behaviour. However, this is currently not available in Code Aster.

The non-linear solver used in Code Aster is a quasi-static calculation in which inertia terms are neglected and a non-physical time component is used to progress the solution from the initial to the final state. The external loads are scaled by the non-physical time step and within each non-physical time step the method of Newton is used to minimise the residual of the membrane equation to a predetermined level of precision.

The membrane surface deformation and stress are output from the non-linear FEA analysis and are used to update the mesh to that of the stressed shape (S in Fig. 1) and for the membrane geometric component of the hydroelastic restoring stiffness, respectively.

III. Dynamic motion analysis

The membrane dynamic response is driven by incident surface gravity waves, which are defined as regular, monochromatic waves travelling in the positive x-direction (Fig. 1). This interaction is known to be a complex high order non-linear process. However, for small amplitude waves and small amplitude body oscillations, it is acceptable to model using a linear approach. By further assuming that the incident waves and device response take a simple harmonic form, varying sinusoidally with the same frequency, then the system may be analysed in the frequency domain. In

that case, the effect of the external and internal domains and the membrane structure itself on the system response can be decomposed into linear excitation force ($\mathbf{F_e}$), mass ($\mathbf{M}$), spring ($\mathbf{K}$) and damping ($\mathbf{B}$) terms related to the membrane modal motion. The device modal amplitude ($\boldsymbol{\xi}$) may be then obtained from the equation

$$\boldsymbol{\xi} = \mathbf{F_e}\left[-\omega^2\mathbf{M} + i\omega\mathbf{B} + \mathbf{K}\right]^{-1}. \tag{1}$$

A. Generalised Modes

The device motion is defined by the linear superposition of mode shapes. To solve (1), these mode shapes must be known in advance to compute the mass, spring, damping and excitation force matrix coefficients. Wave-induced motion on bodies are generally defined by the six rigid body mode shapes, as body deformation is assumed to be orders of magnitude smaller than the rigid body motion. Any analysis of body deformation is then completed separately assuming that the body deformation will not affect the rigid body motion. However, for flexible membrane structures, the body deformation can be of similar magnitude or larger than the rigid body motion such that flexible body modes must also be included.

Flexible mode shapes can easily be added to an analysis by extending rigid body mode shapes to generalised mode shapes (h). Generalised mode shapes are standing waves which define a shape of oscillation (assumed or calculated) of the body in response to excitation. Generalised modes can be used to define rigid body modes, continuous structural deflection modes, and discontinuous hinge modes. While the practical application of each of these generalised mode types are different, mathematically they are dealt with identically. In a computational model, a generalised mode shape is defined by a vector at each node that defines the shape amplitude at that point. The mode shapes should be orthogonal to allow for linear superposition of the mode shapes to determine the total membrane structure response.

The dynamic motion analysis in this model is set up to be agnostic to the type of generalised mode shape used. So that the most appropriate mode shape type can be chosen for each analysis. A number of mode shape types can be used for analysis of membrane deformations

- Orthogonal polynomials
- Dry natural mode shape (computed from membrane mass and stiffness)
- Wet natural mode shapes (computed using the membrane mass and stiffness combined with a contribution to the mass and stiffness from the surrounding water)
- Nodal degree of freedom modes (where the x, y and z motion of each node is a separate mode or can be combined to a single mode in the node normal direction)

B. Hydrodynamic analysis

The hydrodynamic analysis determines the contributions to the excitation force, mass and damping of the generalised modes due to the presence of the waves in the external domain and the induced motion of the fluid in the internal domain. Using the assumption of small amplitude waves and body motions, one can make the assumption of linear potential flow in both the internal and external domain. In the case of potential flow the well known Laplace equation,

$$\nabla^2\phi = 0, \tag{2}$$

is valid in both domains. Where ϕ is the velocity potential, which is related to the water velocity (u) by

$$u = \nabla\phi. \tag{3}$$

The Laplace equation is, however, not sufficient for obtaining a solution. The velocity potential must also satisfy appropriate boundary conditions. These boundary conditions are different for the internal and external domains.

1) External domain: In the external domain, the Laplace equation must satisfy the boundary conditions at the free surface, on the sea-bed, on the surface of each body (either partially or fully submerged in the fluid), and at the far-field boundary.

The linearized boundary conditions in the external domain are

$$\frac{\partial\phi_{ext}}{\partial z} - \frac{\omega^2}{g}\phi_{ext} = 0 \qquad \text{on} \qquad z_{ext} = 0, \tag{4}$$

$$\frac{\partial\phi_{ext}}{\partial z} = 0 \qquad \text{on} \qquad z_{ext} = -d, \tag{5}$$

$$\phi_{ext} \propto (kr)^{\frac{-1}{2}} e^{ikr} \qquad \text{as} \qquad r \to \infty, \tag{6}$$

$$\frac{\partial\phi_{ext}}{\partial n} = u_n \qquad \text{on} \qquad S. \tag{7}$$

Where (7) is the body surface impermeable kinematic boundary condition and u_n is the velocity in the surface normal direction on the body surface.

As linear solutions can be combined by superposition, the velocity potential can be broken down into constituent components; the incident wave field (ϕ_0), the scattered wave field (ϕ_s), and the radiated wave field (ϕ_r) using the equation

$$\phi_{ext} = \phi_0 + \phi_s + \phi_{ext_r}. \tag{8}$$

Where ϕ_0 is the velocity potential due to the incident wave, ϕ_s is the scattered wave velocity potential (obtained by solving the diffraction boundary value problem) and ϕ_{ext_r} is the external radiated wave velocity potential (obtained by solving the radiation boundary value problem). The radiated wave velocity potential is made up of a summation of contributions from each generalised mode, such that

$$\phi_{ext_r} = \sum_{i=1}^{nmodes} \phi_{ext_{r_i}}\xi_i. \tag{9}$$

For the diffraction boundary value problem, the derivative of the total velocity potential normal to the surface is zero, such that the derivative of the scattered potential normal to the surface must be equal and

opposite to that of the incident wave potential normal to the surface,

$$u_n = -\frac{\partial \phi_0}{\partial n}. \tag{10}$$

For the radiation boundary problem, the derivative of the velocity potential normal to the surface is equal to the modal normal velocity. For each mode, this is given by

$$u_{n_i} = \boldsymbol{h}_i.\boldsymbol{n}. \tag{11}$$

2) Internal domain: In the internal domain, the only boundary condition that must be satisfied is the body surface impermeable kinematic boundary condition

$$\frac{\partial \phi_{int}}{\partial n} = u_{n'} \qquad \text{on} \qquad S. \tag{12}$$

Where $u_{n'}$ is the modal normal velocity in the internal domain, which is given by

$$u_{n'_i} = \boldsymbol{h}_i.\boldsymbol{n}'. \tag{13}$$

As there is no incident wave (and so no incident potential or scattered potential) the total velocity potential is made up of the radiated velocity potential only, such that

$$\phi_{int} = \sum_{i=1}^{nmodes} \phi_{int_{r_i}} \xi_i \tag{14}$$

3) Boundary element method: The velocity potential is calculated for both the diffraction and radiation boundary value problem by use of the boundary element method. Using Green's theorem the velocity potential at a point $\boldsymbol{x}$ on the surface can be written in terms of the integral of the source strength (s) at points $\boldsymbol{x}'$ over the body surface.

$$\frac{\phi(\boldsymbol{x})}{2} = -\frac{1}{4\pi} \int_S s(\boldsymbol{x'}) G(\boldsymbol{x}, \boldsymbol{x'}) dS. \tag{15}$$

Where the source strength at a point on the surface is related to the body impermeable condition by the equation

$$2\pi s(\boldsymbol{x}) + \int_S s(\boldsymbol{x}') \frac{\partial G(\boldsymbol{x}, \boldsymbol{x'})}{\partial n(\boldsymbol{x})} dS = u_n. \tag{16}$$

By discretising the body surface and assuming that variables are constant on each panel (with the value at panel centroid used for the entire panel), then (15) and (16) can be discretised to form a linear set of equations for each boundary value problem. These may then be solved for the scattering and radiation potential, to produce the excitation force and the radiation coefficients respectively.

This requires selection of an appropriate Green's function ($G(\boldsymbol{x}, \boldsymbol{x'})$). The Green's function gives the velocity potential at a point $\boldsymbol{x}$ on the surface, due to a point source of strength -4π at another point $\boldsymbol{x'}$. The chosen Green's function must satisfy the Laplace equation and any domain boundary conditions. The difference in boundary conditions for the internal and external domain, therefore lead to the use of different Green's functions. For the external domain, the Green's function is a complex, frequency-dependent function [17]. However, as the internal domain Green's function need only satisfy the surface kinematic condition (12) it can be simplified to a function of the distance between the two surface points [19]

$$G_{int}(\boldsymbol{x}, \boldsymbol{x'}) = \frac{1}{r(\boldsymbol{x}, \boldsymbol{x'})}. \tag{17}$$

Where r is the distance between point $\boldsymbol{x}$ and point $\boldsymbol{x}'$.

This is a significant simplification of the Green's function used for the external domain and, as a result, the internal domain hydrodynamic impedance is imaginary and frequency independent. The result is a single (frequency independent) added mass with zero added damping in the internal domain.

4) Nemoh: Both the internal and external domain, hydrodynamic coefficients are calculated using the open-source BEM software Nemoh [17]. However, it is not possible to perform analysis using generalised mode shapes and analysis of the internal domain using Nemoh as distributed. The Nemoh solver has been written to solve the external domain boundary value problem for any distribution of body surface normal velocities. Thus to allow for analysis of generalised mode shapes one must produce/modify the files generated by the pre-processor with the required generalised mode body surface normal velocities. The files `Normalvelocities.dat`, `Integration.dat`, and `FKforce.dat` are dependant on the mode shape and need to be re-written for the generalised mode surface normal velocities, surface integrals and Froude-Krylov pressures, respectively.

In order to obtain the internal domain added mass some modifications are also required to be made to the Nemoh Solver. The Green's function used in the solver is modified from the frequency dependent term that satisfies the external domain boundary conditions to the frequency independent term which satisfies the body kinematic condition (17). As the internal domain Green's function is a reduced version of the external domain Green's function (see equations (8) and (17) in [17]) this is achieved by setting the relevant terms of the external domain Green's function to zero for the internal domain computation.

C. Hydroelastic restoring stiffness

The complete hydroelastic restoring stiffness [16] is made of components due to the variation in pressure, surface normal direction, boundary stress due to hydrostatic pressure, and stress distribution in the body. The total hydroelastic stiffness for a fluid-filled membrane has to account for hydrostatic stiffness of the internal domain as well as the external domain, and the membrane separating the two domains. In this way, the complete method of Huang and Riggs [16] is extended here to account for the contribution from the internal domain.

In the internal domain, the density of the fluid and the point of zero hydrostatic pressure may be different from the external domain and a constant pressure above hydrostatic (P_0) may also be present. As a result,

the combined internal-external complete hydrostatic stiffness ($\mathbf{K}_{hs}$) becomes

$$\mathbf{K}_{hs} = \mathbf{K}^{P} + \mathbf{K}^{nh} + \mathbf{K}^{s0} + \mathbf{K}^{G}, \tag{18}$$

$$K^{P}_{ij} = \rho_{ext} g \int_S \boldsymbol{h}_i \boldsymbol{h}^z_j \boldsymbol{n} dS + \rho_{int} g \int_S \boldsymbol{h}_i \boldsymbol{h}^z_j \boldsymbol{n'} \mathrm{d}S, \tag{19}$$

$$K^{nh}_{ij} = \rho_{ext} g \int_S Z_{ext} \boldsymbol{h}_i (\nabla \boldsymbol{h}_j) \boldsymbol{n} dS + \rho_{int} g \int_S Z_{int} \boldsymbol{h}_i (\nabla \boldsymbol{h}_j) \boldsymbol{n'} \mathrm{d}S + p_0 \int_S \boldsymbol{h}_i (\nabla \boldsymbol{h}_j) \boldsymbol{n'} \mathrm{d}S, \tag{20}$$

$$K^{S0}_{ij} = -\rho_{ext} g \int_S Z_{ext} (\boldsymbol{h}_i \nabla) \boldsymbol{h}_j \boldsymbol{n} dS - \rho_{int} g \int_S Z_{int} (\boldsymbol{h}_i \nabla) \boldsymbol{h}_j \boldsymbol{n'} \mathrm{d}S - p_0 \int_S (\boldsymbol{h}_i \nabla) \boldsymbol{h}_j \boldsymbol{n'} \mathrm{d}S, \tag{21}$$

$$K^{G}_{ij} = t \int_S \nabla \boldsymbol{h}_i \sigma \nabla \boldsymbol{h} j \boldsymbol{n} dS. \tag{22}$$

Where σ is the stress in the membrane under static loading conditions, output from the static shape analysis.

It should be noted that while Huang and Riggs did not explicitly derive the effect of a constant pressure on the hydrostatic stiffness the description given of the effect in [16] ("if the pressure is constant, rather than varying with depth, then the first term disappears and $\rho g Z$ in the remaining two terms is replaced by the constant pressure") matches the equations derived here.

The internal domain coordinate system is equal to that of the external domain (so that $Z_{ext} = Z_{int}$) if the membrane structure is fully submerged. If the membrane structure protrudes above the free-surface (as in Fig. 1) then the internal domain coordinate system is set to the highest point in the internal domain (assuming no internal free-surface).

D. Membrane dynamics

The membrane linear dynamics are dominated by the membrane mass and stiffness. The generalised mode membrane mass matrix is determined using the equation

$$M_{mem_{ij}} = \int_S \rho_m t \boldsymbol{h}_i \boldsymbol{h}_j \mathrm{d}S. \tag{23}$$

Where ρ_m and t are the membrane density and thickness, respectively. The static shape thickness of each element can be approximated by the change in area from unstressed element area (A_0) to stressed shape area (A_s) relative to the initial thickness (t_0)

$$t = \frac{A_0}{A_s} t_0. \tag{24}$$

The membrane modal stiffness matrix is calculated from the finite element stiffness matrix ($\boldsymbol{K}_e$) as

$$K_{mem_{ij}} = \boldsymbol{h}^t_i \boldsymbol{K}_e \boldsymbol{h}_j. \tag{25}$$

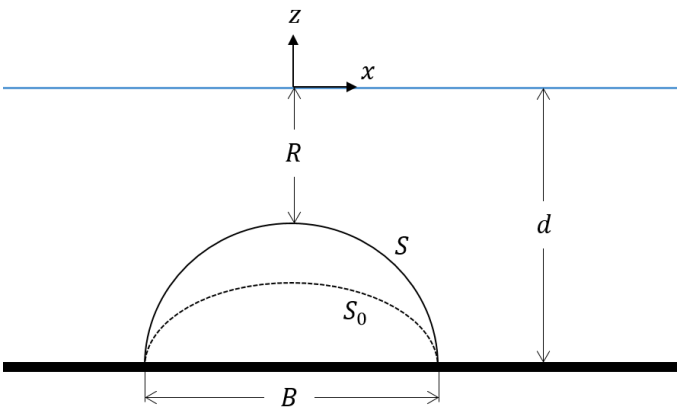

Fig. 2. Cross-section sktech of bottom mounted fluid-filled membrane mound.

Where the finite element stiffness matrix can be calculated using a standard finite element method. In this case, the finite element stiffness matrix is obtained from Code Aster. The finite element mass matrix ($\boldsymbol{M}_e$) can also be obtained from Code Aster so that the membrane dry mode shapes ($\boldsymbol{h}_{dry}$) can be calculated by solving the eigenvalue problem

$$(\boldsymbol{K}_e - \omega^2_{dry} \boldsymbol{M}_e) \boldsymbol{h}_{dry} = \mathbf{0}. \tag{26}$$

IV. Results

This section presents a demonstration of the method described in sections II and III, along with verification by comparison with numerical results of a similar linear numerical model [19] and experimental results [1]. The demonstration case is that of the response of a bottom mounted fluid-filled membrane mound to incident waves. A cross-section of the mound set up is shown in Fig. 2. The experimental test of Ohyama et al. [19] was conducted in a $40m$ long wave tank, with a width of $4m$ and a water depth of $0.8m$. The rubber used for the membrane mound has a Young's modulus, density and thickness of $E = 58kPa$, $\rho_m = 1143kg/m^3$ and $t = 0.00165m$ respectively. The membrane mound base width (B) and length are given as $1.6m$ and $4.0m$. However, the actual dimensions of the membrane used and the shape of the mound sides are not given. The shape of the sides is assumed to be elliptical (unstressed input mesh used is shown in Fig. 3), and the dimensions of the unstressed membrane mound have been chosen such that when the mound is subject to the static load case of the three different internal pressures tested by Ohyama et al. [1] the resulting mound height is similar to that reported for the experimental mound under the same conditions. The comparison of the submergence of the tip of the mound under static load at different internal pressures determined experimentally and using non-linear FEA are shown in Fig. 4.

In order to correctly replicate the hydrodynamics of the experimental study two walls with length $40.0m$ extending from the mean free surface to the seabed were included in the external domain mesh, as shown in Fig. 5.

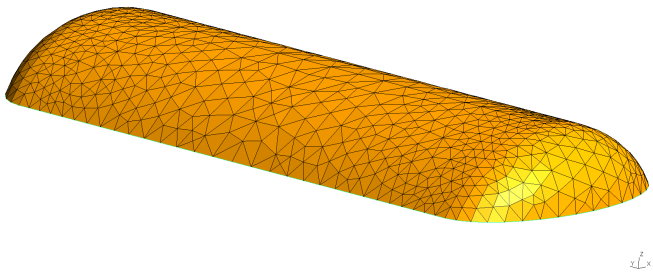

Fig. 3. Input unstressed mound mesh.

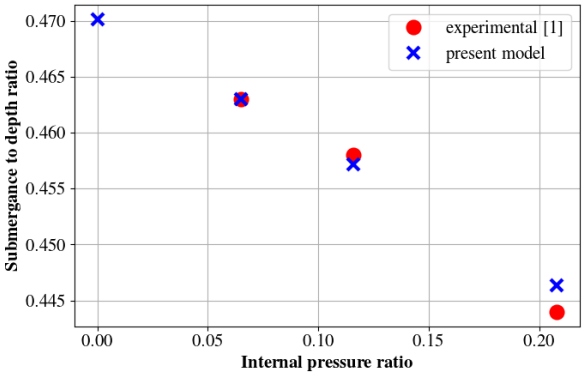

Fig. 4. Ratio of the submergence depth of the mound tip (R/d) as a function of the the internal pressure ratio $(\frac{P_0}{\rho g d})$ from the experimental analysis of Ohyama et al. [1] and the nonlinear FEA analysis performed here using Code Aster [18].

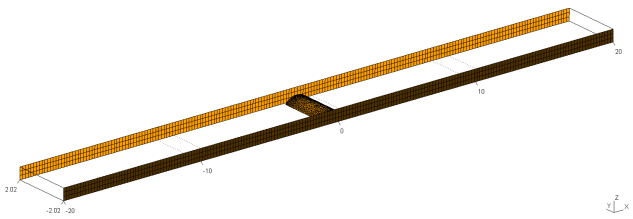

Fig. 5. Mesh used for external domain analysis. Two side walls are separated by $4.04m$ and extend $20m$ to the fore and aft of the mound center-line. The element normals of the two side-walls point towards the x-axis.

For the dynamic analysis, three different types of generalised mode shapes were tested. The analysis was made using orthogonal polynomials (selected based on the known membrane peak responses in the frequency range of interest [1] [9]), dry natural mode shapes and node degree of freedom mode shapes. The main difference between the use of each mode type is the number of generalised modes required. There were three peak response shapes found in the range of interest, so three mode shapes were used for the orthogonal polynomial analysis. For the dry natural mode shapes, it was found that approximately 40 modes were required for convergence of the total structural response. While for the node degree of freedom mode shapes over 1000 modes were required to produce mesh-independent results. The number of mode shapes used has a large impact on the analysis run time as the number of coefficients in each analysis is the square of the number of modes. The orthogonal polynomial modal analysis has the shortest run time and the node degree of freedom modal analysis has the longest run time.

When using the orthogonal polynomial mode analysis, it was found that coefficients based on the membrane global response were well predicted by the polynomials. However, the membrane elastic stiffness (25) was found to be sensitive to the displacement of each node in the mode shape, such that the membrane elastic stiffness was consistently orders of magnitude higher than for a dry natural mode with a similar mode shape. As a result, the response of the membrane was significantly affected and the results were not comparable with the previous numerical or experimental results.

The node degree of freedom mode shapes makes no assumption of the membrane global response prior to analysis and so will provide the full global response (provided there is sufficient mesh refinement) but the run time is prohibitive in this case for full analysis. The dry natural mode shape analysis was therefore found to be the best compromise between accuracy and runtime. Results from the dry natural mode shape analysis are shown in the results that follow.

For direct comparison with the numerical model of Das and Cheung [19], the average response amplitude operator (RAO) over the membrane surface is used. The average response amplitude operator can be calculated from the sum of the mode shapes and response amplitudes as

$$RAO_{ave} = \frac{1}{S}\int_{S_0} | \sum_{i}^{no.modes} (\boldsymbol{h}_i.\boldsymbol{n})\xi_i | dS. \qquad (27)$$

This is calulated for the results generated here and is compared with the numerical model of Das and Cheung [19] in Fig. 6. It can be seen that there is reasonable agreement with the equivalent model of Das and Cheung, with some difference in the frequency of the second and third peak response. The comparison of the results with different internal overpressures highlights the importance of an appropriate restoring stiffness method. It can be seen that as the initial internal overpressure is increased from $\frac{P_0}{\rho g d} = 0.065$ to $\frac{P_0}{\rho g d} = 0.208$ the main difference in the response of the system is an increase in the frequency of the peak responses due to an increase in the stiffness. This increase in stiffness is captured by the increase in the geometric component of the hydroelastic restoring stiffness (22) due to an increase in static stress. This would not be captured by the consistent hydroelastic restoring stiffness method.

There was no measurement of the device response in the experimental study of Ohyama et al. [1], instead, the wave height was measured at two arrays of wave gauges. One array, fixed at $4.0m$ downstream from the mound, was used to calculate the transmission coefficients. While a second moveable array of wave gauges was used upstream of the mound to calculate the reflection coefficients using Healy's method [20]. In the present analysis, the scattered and radiated free surface elevations are obtained using Nemoh. These are then used to calculate the wave transmission and

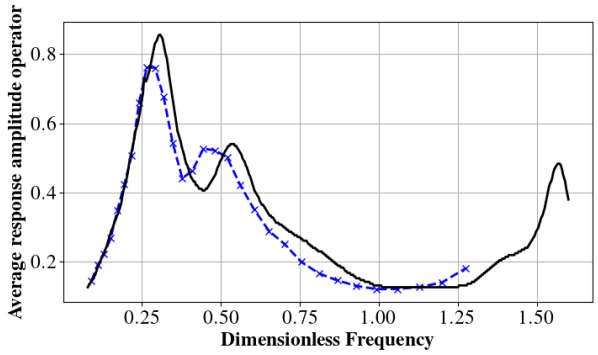

(a)

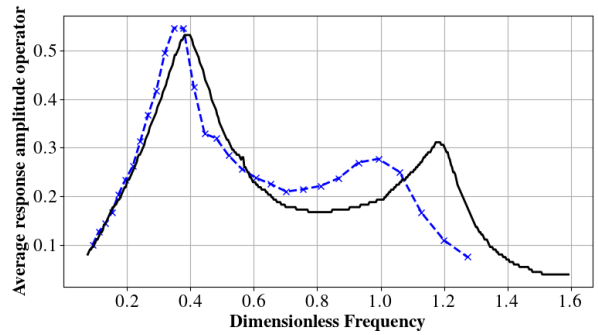

(b)

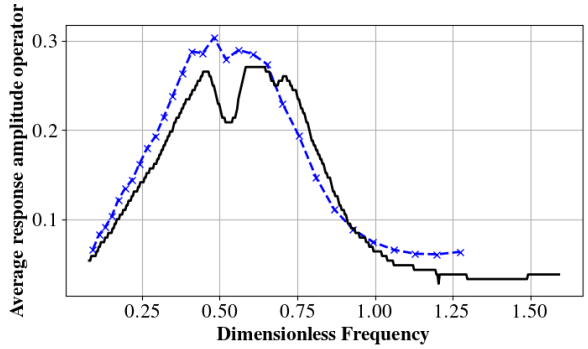

(c)

Fig. 6. Average RAO of fluid-filled membrane mound as a function of dimensionless frequency (B/λ) at internal static pressure (a) $\frac{P_0}{\rho g d} = 0.065$, (b) $\frac{P_0}{\rho g d} = 0.116$, (c) $\frac{P_0}{\rho g d} = 0.208$ (blue dashed line: present model, black solid line: numerical model of Das & Cheung [18]).

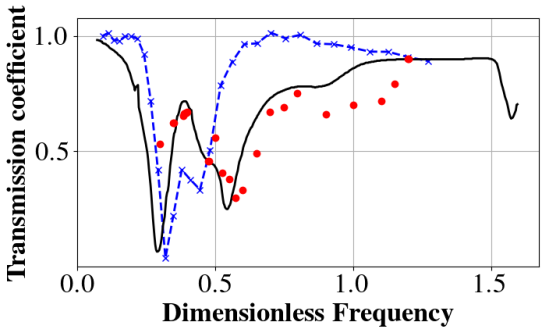

(a)

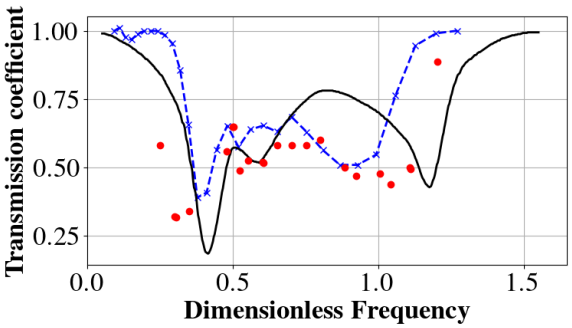

(b)

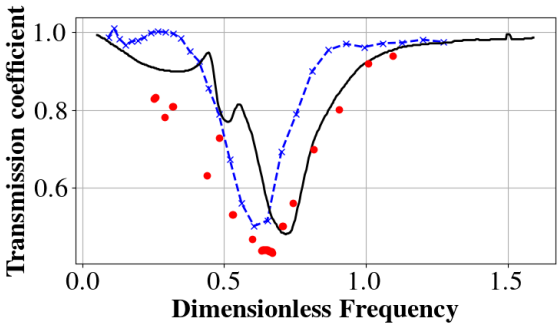

(c)

Fig. 7. Transmission coefficient as a function of dimensionless frequency (B/λ) at internal static pressure (a) $\frac{P_0}{\rho g d} = 0.065$, (b) $\frac{P_0}{\rho g d} = 0.116$, (c) $\frac{P_0}{\rho g d} = 0.208$ (blue dashed line: present model, black solid line: numerical model of Das & Cheung [18], red dot: experimental model of Ohyama et al. [1]).

reflection coefficients. The transmission coefficients are compared with the experimental results of Ohyama [1] and the numerical analysis of Das and Cheung [19] in Fig. 7. It can be seen that neither numerical model completely captures the experimental results of Ohyama et al. But that both provide a reasonable agreement with the wave transmission measured over the bottom-mounted fluid-filled membrane mound.

V. Conclusion

It has been shown how generic fluid-filled membrane structures can be analysed using generalised modes in the frequency domain. The developed model calculates the membrane static shape using a modified nonlinear FEA code, the internal and external domain dynamics are analysed using a BEM code modified to compute generalised mode coefficients for both domains, the effect of the membrane dynamics are accounted for and a restoring stiffness which accounts for the static shape stress in the membrane has been used. The importance of which has been shown by comparison with previous numerical and experimental studies. The effect of the separate domains and the membrane are coupled by the use of generalised modes throughout the dynamic analysis. The model has been developed to allow for a range of mode shape types to be used depending on the analysis being performed, which helps make the method applicable to a wide range of fluid-filled membrane structures. In this case, the dry mode shapes were most appropriate for the structure being analysed, but this may not always be the case. The use of generalised modes also allows for ease of addition, or exchange of, physical processes.

The calculation of the internal domain added mass coefficients for each generalised mode could be exchanged for the compressibility of air in the internal domain on each mode, or a PTO could be included by addition of damping to specific modes. In this way, the model presented here could be extended to model generic flexible membrane wave energy converters.

ACKNOWLEDGEMENT

A. McDonald would like to thank his industrial and academic supervisors and Wave Venture.

REFERENCES

[1] T. Ohyama, M. Tanaka, T. Kiyokawa, T. Uda, and M. Murai, "Transmission and reflection characteristics of waves over a submerged flexible mound," *Coast. Eng. Japan*, vol. 32, no. 1, pp. 53–68, 1989.

[2] W. R. Hawthorne, "The early development of the Dracone flexible barge," in *Proccedings Inst. Mech. Eng.*, London, 1961, pp. 52–83.

[3] C. Aadland, "se alt de gjr for f lukket fisken i sjen inne (look at all they do to close the fish cage)," 2015. [Online]. Available: https://sysla.no/fisk/se-alt-de-gjor-for-a-fa-lukket-fisken-i-sjoen-inne/

[4] N. W. Bellamy, A. Bucchi, and G. E. Hearn, "Analysis of the SEA-OWC-Clam wave energy device - Part A: Historical development, hydrodynamic and motion response formulations & solutions," *Renew. Energy*, vol. 88, pp. 220–235, 2016.

[5] Wave Energy Scotland, "Materials Landscaping Study," Wave Energy Scotland, Tech. Rep., 2016.

[6] A. Mcdonald, Q. Xiao, H. Smith, and R. Costello, "Initial development of a generic method for analysis of flexible membrane wave energy converters," pp. 333–340, 2018.

[7] R. Zhao, "A Compleate linear theory for a two dimensional Floating and liquid- filled membrane structure in waves," pp. 937–956, 1995.

[8] R. Zhao and J. V. Aarsnes, "Numerical and experimental studies of a floating and liquid-filled membrane structure in waves," *Ocean Eng.*, vol. 25, no. 9, pp. 753–765, 1998. [Online]. Available: http://linkinghub.elsevier.com/retrieve/pii/S0029801897000139

[9] A. C. Phadke and K. F. Cheung, "Response of Bottom-Mounted Fluid-Filled Membrane in Gravity Waves," *J. Waterw. Port, Coastal, Ocean Eng.*, vol. 125, no. 6, pp. 294–303, 1999.

[10] L. L. Broderick and J. W. Leonard, "Nonlinear water-wave structure interaction," *Comput. Struct.*, vol. 44, no. 4, pp. 837–842, 1992.

[11] A. C. Phadke and K. F. Cheung, "Nonlinear Response of Fluid-Filled Membrane in Gravity Waves," *J. Eng. Mech.*, vol. 129, no. 7, pp. 739–750, 2003.

[12] I. Senjanović, N. Vladimir, M. Tomić, N. Hadžić, and Š. Malenica, "Global hydroelastic analysis of ultra large container ships by improved beam structural model," *Int. J. Nav. Archit. Ocean Eng.*, vol. 6, no. 4, pp. 1041–1063, 2014.

[13] J. N. Newman, *Marine Hydrodynamics*, 40th ed. The MIT Press, 1977.

[14] I. Senjanović, N. Vladimir, and M. Tomić, "Formulation of consistent restoring stiffness in ship hydroelastic analysis," *J. Eng. Math.*, vol. 72, no. 1, pp. 141–157, 2012.

[15] I. Senjanović, N. Hadžić, and M. Tomić, "Investigation of Restoring Stiffness in the Hydroelastic Analysis of Slender Marine Structures," *J. Offshore Mech. Arct. Eng.*, vol. 133, no. 3, p. 031107, 2011. [Online]. Available: http://offshoremechanics.asmedigitalcollection.asme.org/article.aspx?articleid=1457456

[16] L. L. Huang and H. R. Riggs, "The hydrostatic stiffness of flexible floating structures for linear hydroelasticity," *Mar. Struct.*, vol. 13, pp. 91–106, 2000.

[17] A. Babarit and G. Delhommeau, "Theoretical and numerical aspects of the open source BEM solver NEMOH," in *Proc. 11th Eur. Wave Tidal Energy Conf.*, no. Sept 2015, Nantes, 2015, pp. 1–12.

[18] E. de France, "Finite element $code\_aster$, analysis of structures and thermomechanics for studies and research," Open source on www.code-aster.org, 1989–2018.

[19] S. Das and K. F. Cheung, "Coupled boundary element and finite element model for fluid-filled membrane in gravity waves," *Eng. Anal. Bound. Elem.*, vol. 33, no. 6, pp. 802–814, 2009.

[20] J. Healy, "Wave Damping Effect of Beaches," in *Proc. Int. Hydraulics Convention*, Minnesota, 1952, pp. 213–220.